Resolution dependence of magnetosheath waves in global hybrid-Vlasov simulations

Maxime Dubart[1], Urs Ganse[1], Adnane Osmane[1], Andreas Johlander[1], Markus Battarbee[1], Maxime Grandin[1], Yann Pfau-Kempf[1], Lucile Turc[1], and Minna Palmroth[1,2]

[1]Department of Physics, University of Helsinki, Helsinki, Finland
[2]Space and Earth Observation Centre, Finnish Meteorological Institute, Helsinki, Finland

Correspondence: Maxime Dubart (maxime.dubart@helsinki.fi)

Abstract. Plasma waves are ubiquitous in the Earth's magnetosheath. The most commonly observed waves arise from instabilities generated by temperature anisotropy of the ions, such as the mirror and proton cyclotron instabilities. We investigate here the spatial resolution dependence of the mirror and proton cyclotron instabilities in a global hybrid-Vlasov simulation using the Vlasiator model. We compare the proton velocity distribution functions, power spectra and growth rates of the instabilities

5 in a set of simulations with three different spatial resolutions but otherwise identical set-up. We find that the proton cyclotron instability is absent at the lowest resolution and that only the mirror instability remains, which leads to an increased temperature anisotropy in the simulation. We conclude that the proton cyclotron instability is resolved well enough at the highest spatial resolution and that an increase of resolution does not improve the resolution of the instability enough to justify this increase at the cost of numerical resources in future simulations. We also find that a resolution around 0.6 the inertial length in the

10 solar wind, presents an acceptable minimum spatial resolution in which the proton cyclotron is still correctly resolved. These results should be taken into consideration regarding the optimal grid spacing for the modelling of magnetosheath waves, within available computational resources.

1 Introduction

The Earth's magnetosheath is permeated with several kinds of ion-kinetic waves, which are an important source of energy trans-

15 fer and dissipation within the magnetosheath plasma (Schwartz et al., 1997). The most commonly observed waves arise from instabilities generated by temperature anisotropy of the ions. The mirror instability (Chandrasekhar et al., 1958; Hasegawa, 1969; Southwood and Kivelson, 1993; Kivelson and Southwood, 1996) and the proton cyclotron instability (Davidson and Ogden, 1975; Gary et al., 1993) are excited by a temperature anisotropy where the ions' perpendicular temperature $T_\perp$ is larger

20 than the parallel temperature $T_\parallel$.

The mirror instability gives rise to compressional, linearly polarised, waves characterised by zero frequency in the plasma frame, anti-correlation between the plasma density and the magnetic field, and magnetic perturbations which are mostly parallel

to the background magnetic field. They create magnetic mirror-like structures trapping particles (Soucek et al., 2008). Mirror modes are dominant in high plasma beta (Tsurutani et al., 1982). The proton cyclotron instability has maximum growth rate

25 around the ion cyclotron frequency, and produces waves propagating in the direction parallel to the background magnetic field. The magnetic perturbations of the waves are perpendicular to the background magnetic field and produce left-handed circularly polarised waves in the plasma frame (Davidson and Ogden, 1975; Lacombe et al., 1994). The proton cyclotron instability is dominant in low beta plasma (Gary, 1992).

The mirror and proton cyclotron instabilities have been observed in the Earth's magnetosheath (Tsurutani et al., 1982; An-

30 derson et al., 1996; Gary et al., 1993; Soucek et al., 2008) as well as in the solar wind (Hellinger et al., 2006) and sheath regions driven by coronal mass ejections (Ala-Lahti et al., 2019). Both instabilities isotropize the ion populations of the magnetosheath by pitch angle scattering the protons (Hasegawa, 1969; Tanaka, 1985), thus reducing the temperature anisotropy of the population. The proton cyclotron instability isotropizes ions faster than the mirror instability (McKean et al., 1992). These properties have been studied through simulations by, e.g. McKean et al. (1994); Gary and Winske (1993); Seough et al.

35 (2015); Hoilijoki et al. (2016). However, these simulations were either one-dimensional (Gary and Winske, 1993) or used a particle-in-cell approach (Seough et al., 2015), and apart from Hoilijoki et al. (2016), none of them studied the instabilities in a global simulation of Earth's magnetosheath. Hoilijoki et al. (2016) focused only on the mirror instability. These simulations did not study the impact of the spatial resolution on the description of the instabilities.

Modern plasma physics is increasingly relying on the support of numerical simulations in understanding waves and insta-

40 bilities. Whether it is used for the study of laboratory plasmas (Revel et al., 2018), nuclear fusion (Görler et al., 2011) or space plasmas (McKean et al., 1994), numerical modelling of instabilities is crucial for the understanding of the physics of the system. However, no matter what kind of numerical model is chosen, it is difficult to model the entire system at a numerical resolution capturing both large-scale and small-scale physical processes involved without incurring a very high computational cost. The issue is even more relevant when global simulations of large systems are carried out, for physical understanding or

45 for space weather forecasting (Palmroth et al., 2018; Pomoell and Poedts, 2018). The choice of resolution is a central parameter in numerical models, and often presents a tradeoff between accuracy and computational cost. To be able to make an informed choice about this tradeoff, a firm understanding of the impact of the models' resolution on the physical processes at play in the system is required.

In order to model the processes involved in energy transfer and dissipation, the understanding of the instabilities generating

50 them is essential. In this study, we investigate the impact of the spatial resolution on the ion-scale waves produced by the mirror and proton cyclotron instabilities in a 2D global hybrid-Vlasov simulation of the Earth's magnetosphere using the Vlasiator model (Palmroth et al., 2013; von Alfthan et al., 2014; Palmroth et al., 2018). A study by Pfau-Kempf et al. (2018) showed that, for 1D simulations of oblique shocks, a coarse resolution in Vlasiator such as cells of size $\Delta r = 1000$ km was still sufficient to describe correctly most of the kinetic effects related to shocks. Despite not resolving the ion skin depth of 228 km in this

55 simulation, the results were similar to a simulation with a spatial resolution of $\Delta r = 200$ km, where the ion skin depth is resolved. Ions velocity distribution functions obtained by the Vlasiator model at coarse resolution are also consistent with observations (Kempf et al., 2015). However, the effect of spatial resolution on the description of plasma instabilities in 2D

global kinetic simulations is still an open question. The spatial resolution of a simulation impacts the evolution of the fields during the simulation. Therefore, it will modify the development of the different instabilities present in the magnetosheath and their effect on the velocity distribution functions. In this paper, we determine the lowest possible spatial resolution which can still be used to model the mirror and proton cyclotron instabilities in a 2D global simulation. This allows computational resources to be used more efficiently when global hybrid-Vlasov simulations of near-Earth space are expanded to the third dimension. We focus this investigation on the magnetosheath waves downstream of the quasi-perpendicular shock, as they are well defined and less perturbed by the shock processes than downstream of the quasi-parallel shock. We decided to focus on the proton cyclotron and mirror instabilities as their properties are well documented and are a good proxy for their dependence on the resolution.

2 Global hybrid-Vlasov model

We performed this study using the Vlasiator model. Vlasiator is a global hybrid-Vlasov model (Palmroth et al., 2013; von Alfthan et al., 2014; Palmroth et al., 2018). Currently, it consists of a cartesian 2D spatial grid containing the nightside and dayside of the Earth's magnetosphere, magnetosheath, bow shock and foreshock. A cartesian 3D velocity space grid is coupled with each of the ordinary space cells. The model solves the time evolution of the protons in phase space by solving the Vlasov equation, coupled with the electric and magnetic fields. The fields are propagated using Maxwell's equations. Closure of the system is performed with the generalised Ohm's law including the Hall term. In each grid cell, the protons are discretised as velocity distribution functions (VDFs). Electrons are considered a cold, massless, charge-neutralising fluid. The Vlasiator model, and global hybrid-Vlasov simulations in general, have the advantage to be noise-free (Palmroth et al., 2018).

The Vlasiator model can be run in 1D, or 2D in ordinary space. In this study we investigate the ion-scale waves produced by the proton cyclotron and mirror instabilities in three 2D simulations with different spatial resolutions but otherwise identical set-up. Typically, in 2D Vlasiator simulations, the spatial resolution of the grid in ordinary space is set to $\Delta r = 300$ km (e.g. Blanco-Cano et al., 2018; Grandin et al., 2019; Hoilijoki et al., 2019), which corresponds to $\Delta r = 1.32\, d_i$, the proton skin depth. Simulations with resolution of $\Delta r = 228$ km $= 1\, d_i$ have also been used (e.g Palmroth et al., 2018; Turc et al.). When extending simulations to 3D, such a high resolution may become unfeasible, even when using adaptive mesh refinement for regions of interest.

In order to study the effect of spatial resolution on magnetosheath waves, we conducted three simulations using the same set-up, with different spatial resolution: $\Delta r = 300, 600,$ and 900 km, which corresponds to $\Delta r = 0.76, 0.38$ and $0.25\, d_i$ in the solar wind, respectively. The system is in the geocentric solar ecliptic (GSE) coordinate system, assuming a zero magnetic dipole tilt. All runs are 2D, describing the noon-midnight meridional plane (X-Z) of near-Earth space. The real-space boundaries of the simulations extend from $X = -48\,\mathrm{R_E}$ in the nightside to $X = 64\,\mathrm{R_E}$ in the dayside, and from $Z = -60\,\mathrm{R_E}$ to $Z = 40\,\mathrm{R_E}$ in the north-south direction, asymmetrical to accommodate the foreshock in the negative Z-direction, with $\mathrm{R_E} = 6371$ km the Earth radius. The north, south and nightside boundaries all apply von Neumann boundary conditions. The inner boundary is located at $4.7\,\mathrm{R_E}$ from the centre of the Earth and consists of a perfectly conducting sphere. The homogeneous and constant

Annales
Geophysicae
Discussions

solar wind is flowing from the dayside boundary in the $-X$ direction with a velocity of 750 km/s, interplanetary magnetic field (IMF) strength of 5 nT, and temperature of 0.5 MK. The IMF makes an angle of $45°$ with respect to the X direction, southward. The solar wind protons are represented by a Maxwellian distribution function, with density 1 cm^{-3}, and a velocity space resolution of 30 km s^{-1}. This setup is identical to the one used in Blanco-Cano et al. (2018).

95   Figure 1 displays a global overview of the magnetic field magnitude in the dayside of near-Earth space in the three different runs. One can identify the upstream solar wind (in dark blue), the bow shock, the magnetosheath and the magnetosphere (mostly yellow). The white circle of radius 4.7 R$_{\mathrm{E}}$ represents the inner boundary of the simulation. The white square indicates the portion of the simulation we will focus on in this study. One can already notice differences in the magnetosheath wave properties as a function of the resolution of the three different setups. For example, we can observe stripes of roughly constant

100   magnetic field strength in the 300 km run. These structures are larger in the 600 km run, and have almost disappeared in the 900 km run.

3 Results: Ion-scale waves

3.1 Alfvén waves and mirror modes

In order to identify the resolved wave modes in the different runs, we use the 2D Fast Fourier Transform (FFT) analysis.

105   Figure 2 displays the wave power of the electric field component in the GSE y direction (i.e. the out-of-plane direction), in the simulation frame, as a function of the frequency ω normalised to the ion cyclotron frequency $\Omega_c = qB/m_p$, and the wave vector $\mathbf{k}$ parallel to the average magnetic field over the time and space intervals in panels (a), (c) and (e), and perpendicular in panels (b), (d) and (f). This analysis is performed in a square extending from $X = 3$ R$_{\mathrm{E}}$ to $X = 6$ R$_{\mathrm{E}}$ and from $Z = 15$ R$_{\mathrm{E}}$ to $Z = 18$ R$_{\mathrm{E}}$, depicted in red in Fig. 1, during a time interval from 800 s to 1200 s of the simulation. The maximum possible $\mathbf{k}$,

110   the Nyquist wave number, depends on the spatial resolution Δr of the simulation as $k_{\max} = \pi/\Delta r$, hence a smaller $k_{\max}$ at lower resolution. The x-axis is normalised to the ion inertial length given by $d_i = \sqrt{m_p \epsilon_0 c^2/(nq^2)}$, where m_p is the proton mass, ϵ_0 the vacuum permittivity, c the speed of light, n the local proton number density in the magnetosheath, and q the proton charge. The solid black lines indicate the Courant-Friedrichs-Lewy (CFL) condition. The CFL condition is a necessary condition for the convergence of the solution in a model and depends on its spatial and temporal resolutions, implying that no

115   signal can propagate more than one spatial cell within one time interval of the simulation. This means that all features found in between the two black lines are beyond the resolution of the simulation and probably result of numerical features.

    At the highest resolution, the dominant wave mode observed in Fig. 2a (i.e. $k_{\parallel} d_i \approx -0.4$, $\omega/\Omega_{ci} \approx 1.0$) matches the Alfvén velocity $v_A = B/\sqrt{\mu_0 \rho_m}$ (Alfvén, 1942), indicated by solid blue lines, where B is the magnetic field, μ_0 the vacuum permeability and ρ_m the mass density of protons. This wave mode is propagating almost entirely in the anti-parallel direction,

120   as evidenced by the much smaller wave power along the Alfvén velocity in the perpendicular direction (Fig. 2b). Since the plasma flow in the magnetosheath is super-Alfvénic, two curves describing the Alfvén velocity appear on the left side of Fig. 2a: the upper solid blue curve describes the waves propagating in the direction anti-parallel to the magnetic field in the plasma frame, while the lower solid blue curve describes the waves propagating in the direction parallel to the magnetic field in the

Annales
Geophysicae
Discussions

EGU Open Access

plasma frame. These ones appear on the $k_\parallel < 0$ side of the plot, because of the Doppler shift $\omega' = \omega - \mathbf{k} \cdot \mathbf{V}$, where $\mathbf{V}$ is the

125 plasma bulk velocity. As in observations from Zhao et al. (2020), we see both parallel and anti-parallel propagating waves at the same time. The anti-parallel propagating waves are dominant, as an instability will generate waves propagating in both directions. The wave mode in Fig. 2a extends up to the proton cyclotron frequency. Figures 2c and 2d show similar features: the observed waves are the same as in Fig. 2a, matching the Alfvén velocity, except that their excitation seems to be constrained to frequencies below $\approx 0.7\ \omega_{ci}$. Now for the lowest resolution case, displayed in Fig. 2e and 2f, it appears that the features present

130 in the two higher-resolution simulations are completely absent. The waves around the cyclotron frequency are most likely not resolved at this resolution.

Figure 3 displays the wavelet power spectra obtained from wavelet analysis (Torrence and Compo, 1998) of the out-of-plane component of the magnetic field during the interval of time when the FFTs were performed, taken at the virtual spacecraft locations indicated by a black and white circle in Fig. 1. The frequency of the main wave mode at the highest resolution in

135 panel (a) fluctuates around the proton cyclotron frequency $f_{ci} = \Omega_c/2\pi$ shown with a black line, as observed in Fig. 2a. In panel (b), the waves are still present around the cyclotron frequency but the wave power is lower, as observed in Fig 2c, most likely due to the lower resolution. They are completely absent at the lowest resolution in panel (c), as only very low frequency waves below the cyclotron frequency can be observed.

The polarisation of the magnetic field taken at the virtual spacecraft locations indicated in Fig. 1 is also analysed using

140 the minimum variance analysis (Sonnerup and Scheible, 1998), and the results are displayed in Fig. 4a-d. These hodograms display the magnetic field fluctuations during 18 s. The wave vector is along the minimum variance direction δB_N. Figures 4a and 4b highlight that, at $\Delta r = 300$ km, the wave displays few to no perturbations in the parallel direction to the magnetic field (panel (a)), and is left-handedly polarised (panel (b)) in the simulation frame. The angle between the wave vector $\mathbf{k}$, obtained from minimum variance analysis, and the ambient magnetic field is $\theta_{kB} = 15°$. This can be assumed to be a nearly parallel

145 propagation. Based on Fig. 2, we find that these waves move along the plasma flow. The frequency of the waves in the plasma frame is given by $\omega' = \omega - \mathbf{k} \cdot \mathbf{V}$. Therefore, a Doppler shift will not change the sign of ω and the polarisation is the same in the plasma frame. Figures 4c and 4d highlight an identical behaviour of the wave at lower resolution $\Delta r = 600$ km. We don't perform a minimum variance analysis on the third run at $\Delta r = 900$ km because there is no significant wave activity around the ion cyclotron frequency. However, we display the fluctuations of the magnetic field and the proton density at the position

150 indicated in Fig. 1c for the time interval considered in the study in Fig. 5. This indicates that they are anti-correlated and would suggest the presence of mirror waves (Hoilijoki et al., 2016).

To further analyse how the spatial resolution impacts the different wave modes, we investigate the growth rates of the waves. We use the numerical dispersion solver HYDROS (HYbrid Dispersion RelatiOn Solver) (Told et al., 2016), designed for hybrid kinetic plasmas. The solver assumes a bi-Maxwellian proton distribution function, and we input the ion parallel temperature,

155 the ion temperature anisotropy, and the ion parallel beta in the magnetosheath of the different simulations, taken at the same locations as the data for the wavelet analysis, indicated in Fig. 1, averaged over the time range of the study. The electrons are modelled as a fluid. The propagation angle between the wave vector and the magnetic field vector is set to zero for parallel propagation. Figure 6a displays the growth rate γ of the proton cyclotron instability for the three different resolutions. The

Annales
Geophysicae
Discussions

theoretical maximum wave vector is $k_{\max} = \pi/\Delta r$. However, a signal modelled by such $k_{\max}$ would be described with only two points per wavelength. Slightly more realistic is the assumption that a wave needs to be modelled with at least four cells per wavelength. Hence, we consider that the minimum wavelength the model can resolve at each resolution is $\lambda_{\min} = 4\Delta r$, which corresponds to a maximum wave vector $k_{\max} = \pi/2\Delta r$. This wave length is displayed by vertical dashed lines. The growth rates are consistent with what is observed in Fig. 2: at $\Delta r = 300$ km, the growth rate for the proton cyclotron instability is almost fully within the resolved wave length domain. At $\Delta r = 600$ km, only the low-wavenumber edge of the growth rate curve is resolved, below $k_\parallel d_i \approx 0.35$, which is consistent with where the wave power vanishes in Fig. 2c. At $\Delta r = 900$ km, the growth rate curve is completely outside the resolved domain. This would explain why the wave around the proton cyclotron frequency are not observed in this run. We also notice that the maximum growth rate is dependent on the resolution of the simulation, maximum being higher at lowest resolution, because of higher temperature anisotropy. Figure 6b displays the growth rate of the mirror instability for the three different resolutions. We used the same input parameters as for the proton cyclotron instability, except that we set the propagation angle to $45°$, and frequency to zero. At $\Delta r = 300$ km, the growth rate is fully into the resolved domain, but at the very low rate. It is higher for the two other resolutions, even though only resolved partially.

Figure 7 displays the temperature anisotropy in the three different runs considered in the study. The anisotropy grows downstream of the quasi-perpendicular bowshock. For $\Delta r = 300$ km in panel (a), waves reduce the anisotropy quickly in the middle of the magnetosheath. We have found that waves with a frequency around the proton cyclotron frequency are present at this resolution. For $\Delta_r = 600$ km in panel (b), the anisotropy is reduced but at a much slower rate. At this resolution, the waves at the proton cyclotron frequency had a lower wave power. In panel (c), at $\Delta r = 900$ km, a strong anisotropy persists for more than 5 R_E, and even after some isotropization has taken place, a high anisotropy of values around 3 remains.

3.2 Velocity distribution functions

Figure 8 displays the magnitude of the magnetic field in a zoomed portion of the simulation in the magnetosheath, downstream of the quasi-perpendicular shock, indicated by the white square in Fig. 1, with velocity distribution functions (VDF) taken from the point marked by the black and white circle (see Fig. 1), for the three different resolutions. In Fig. 8a, small wavelength waves (of the order of 0.2 R_E) are distinguishable. These are the waves with frequency around the proton cyclotron frequency identified in the previous section. In addition, larger wavelength structures (of the order of 1 R_E) are observed, becoming larger in Fig. 8e, and becoming distinct magnetic field enhancements in Fig. 8i. These structures appear to be convected with the plasma flow, as shown by the animated version of Figure 1 (see Supplementary Video), and are consistent with the mirror modes identified in the previous section. On the right, three slices of the VDFs through the velocity space in different planes are presented. All velocities are transformed to the local plasma frame. Panels (b), (f) and (j) display the slice in the $(\mathbf{v_B}, \mathbf{v_{B \times V}})$ plane. Panels (c), (g) and (k) display the $(\mathbf{v_{B \times V}}, \mathbf{v_{B \times (B \times V)}})$ plane. Panels (d), (h) and (l) display the $(\mathbf{v_B}, \mathbf{v_{B \times (B \times V)}})$ plane. On panels (b), (c) and (d), corresponding to the $\Delta r = 300$ km resolution, one can identify nearly Maxwellian VDFs in all three directions, which is consistent with observations (Williams et al., 1988). In panels (f), (g) and (h), at $\Delta r = 600$ km, the VDFs have a nearly Maxwellian shape in all three directions, with the beginning of the development of a small loss cone in the parallel

direction. At the lowest resolution $\Delta r = 900$ km, in panel (i), the smaller wavelength structures which can be observed in the background of panel (a) have disappeared, with only large structures remaining. Moreover, the associated VDFs in panels (j)

195 and (l) have an "hourglass" shape, in contrast to the nearly Maxwellian shape in panels (b), (c) and (d). The 600 km case in panels (e)-(h) can be considered an intermediate case.

4   Discussion

In this paper, we use Vlasiator simulations of near-Earth space with three different spatial resolutions to investigate the behaviour of the proton cyclotron and the mirror instabilities and their dependence on these resolutions. We used 2D-FFT and

200 wavelet analysis in order to identify the waves produced by these instabilities, their different properties at the different resolutions, and the impact of these different properties on the velocity distribution functions of the protons. The growth rate of the proton cyclotron instability at the different resolutions is calculated and compared with resolution-dependent minimum wavelengths. The temperature anisotropy in the magnetosheath of the different run is analysed.

As Fig. 2, 3 and 4 illustrate, the higher frequency waves propagate with the Alfvén velocity, in the parallel direction, with

205 perpendicular perturbations which are left-handed polarised, with frequency around the ion cyclotron frequency. This suggests that the wave mode present at the 300 km and 600 km resolutions is the Alfvén ion cyclotron wave mode (AIC waves) (Anderson et al., 1996; Rakhmanova et al., 2017), or also known as electromagnetic ion cyclotron (EMIC) waves. In the 900 km case, the AIC waves are not present. In addition, the magnetic field and density perturbation analysis shown in Fig. 5 suggest that mirror modes are present in the 900 km case, which appear to be the dominant wave mode at this spatial resolution.

210 A more detailed study about mirror modes in Vlasiator has been conducted by Hoilijoki et al. (2016).

The growth rate analysis shown in Fig. 6a suggests that the AIC waves are well resolved in the 300 km resolution run, with the highest resolution used in this study. Along with the proton cyclotron instability, Hoilijoki et al. (2016) showed that the mirror instability was also resolved in the simulation. The 600 km resolution case seems to limit the frequency of the waves below the ion cyclotron frequency, while still partially resolving the AIC waves, whereas the 900 km run highlights that only

215 mirror modes are present in the magnetosheath and shows no sign of the AIC waves, as pointed out by Fig. 2 and 3, since the resolution of the simulation does not allow the Alfvén mode to grow sufficiently (Fig. 6). Figures 8a and 8i can be compared with Fig. 3 and 6 of McKean et al. (1994), although the disappearance of the proton cyclotron instability is not due to the spatial resolution in their study. They included Helium ions in their simulation, which tend to suppress the proton cyclotron instability, with only the mirror instability remaining, resulting in similar magnetosheath wave properties as in our 900 km

220 resolution run. The growth rate analysis of the mirror instability shown in Fig. 6b suggests that the mirror modes barely grow in the middle of the magnetosheath, were the data were taken, for $\Delta r = 300$ km. Since Hoilijoki et al. (2016) shown that they are still present, they probably grow near the quasi-perpendicular bowshock, where the temperature anisotropy is higher, and then travel with the plasma flow. The proton cyclotron instability however grows much faster and isotropize the ions (Davidson and Ogden, 1975; McKean et al., 1992). At $\Delta r = 600$ km, the mirror instability has a larger growth rate than at $\Delta r = 300$ km,

225 but still lower than the proton cyclotron instability. Both instabilities grow, the proton cyclotron instability is more efficient tp

isotropize ions than the mirror instability, but cannot develop completely, hence the beginning of a loss-cone observed in Fig. 8f and Fig. 8h. At the lowest resolution, both instabilities should grow. However, the spectrum of wave vectors triggered by the instabilities are not broad enough to scatter particles and thermalise the plasma. Therefore, we believe no instability grows in the middle of the magnetosheath at this resolution.

230   The absence of the Alfvén mode at lower resolution leads to the discrepancies on the VDFs depending on the spatial resolution. Panels (b)-(d) of Fig. 8 show that, in the higher resolution case, the VDFs appear to have a nearly bi-Maxwellian shape, which is still partially present in panels (f)-(h) at $\Delta r = 600$ km, until this shape is deformed into an "hourglass" shape at the lowest resolution in panels (j)-(l). This shape suggests the presence of a loss-cone instability (Ichimaru, 1980), produced by mirror modes like structures. However, the growth rate of this instability is too slow to develop further. Particles cannot
235   be scattered by the AIC waves, which are absent at low resolution, and hence the particles are trapped within the mirror modes. Therefore we observe a loss-cone in pitch-angle in the VDFs at this resolution. This loss-cone does not appear at the highest resolution, as the AIC waves dominate the wave-particle interaction when both instabilities are present (McKean et al., 1994). The VDFs shown in Fig. 8 are representative of those observed throughout the studied time range, as can be seen in supplementary videos.

240   Figure 7 displays the temperature anisotropy of the global simulation at the three different resolutions. The consequence of the absence of the AIC waves can be observed as a higher temperature anisotropy of the magnetosheath at the lowest resolution. Fig. 7 indicates that the temperature anisotropy grows larger as the spatial resolution of the simulation decreases. The AIC waves isotropize VDFs faster than the mirror modes, reducing the temperature anisotropy (Davidson and Ogden, 1975; McKean et al., 1992).

245   Unresolved waves lead to energy transfer processes which are not being properly simulated, and hence lead to larger temperature anisotropies. One could argue that an easy way to get rid of this issue and to resolve physics beyond the ion inertial length (eg. kinetic Alfvén waves) would be to use a spatial higher resolution. We conducted a similar study for a spatial resolution $\Delta r = 227$ km (this simulation was also used in Hoilijoki et al. (2016)), which resolves the ion inertial length, and shows no evidence of new phenomena or wave modes, nor a better modelling of the ones already present at $\Delta r = 300$ km.
250   High-resolution simulations are numerically costly, and therefore are not feasible globally in this fine resolution for the entire volume. This is especially true in large simulations such as global 6D simulations (3D real-space grid and 3D velocity-space grid) which will require adaptive mesh refinement allowing to focus resolution on regions of interest and decrease the resolution and computational cost significantly elsewhere. For our solar wind driving parameters, the ion skin depth is 227.7 km. We find that, despite not fully resolving the inertial length, the resolution $\Delta r = 300$ km leads to well resolved proton cyclotron
255   and mirror instabilities. Since they are the two main competing instabilities in magnetosheath plasmas (Anderson and Fuselier, 1993; Gary, 1992; Soucek et al., 2015), we find that the resolution $\Delta r = 300$ km had sufficient resolution to correctly resolve these waves in the magnetosheath. We also find that even at the lower resolution $\Delta r = 600$ km, the proton cyclotron instability still produces left-handed circularly polarised waves, and almost bi-Mawellian VDFs. Therefore we believe that an acceptable minimum spatial resolution in a simulation to study magnetosheath waves would lie between $\Delta r = 300$ and 600 km. Based
260   on Fig. 6, we suggest that a spectrum of wave vectors $k * d_i$ up to 0.5 would be large enough to allow the proton cyclotron

instability to grow sufficiently to produce well resolved AIC waves and correctly model the isotropization processes. This would correspond to a maximum resolution of $\Delta r \approx 440$ km, around $0.6\ d_i$ in the solar wind.

It is evident that one can make a choice of spatial resolution depending on which waves are wanted in the simulation. However, in case of large-scale simulation volumes where the entire simulation box cannot be represented with a uniform

265   grid resolution, it is interesting to contemplate whether one can use a sub-grid model to reproduce the most important wave modes at the coarser grid volumes. A future topic of study would be to design an empirical model based on the results we have presented here in this article, in order to modify the VDFs to a more Maxwellian shape, or to solve the Vlasov equation with adding a diffusion term at lower resolution in order to mimic the energy dissipation mechanisms at work at smaller scales.

5 Conclusions

270   This paper presents an investigation into the spatial resolution dependence of two proton instabilities in a global hybrid-Vlasov model. Three 2D simulations of the near Earth-space at different spatial grid resolutions are carried out, and the effects on the produced magnetosheath waves and velocity distribution functions downstream of the quasi-perpendicular shock are investigated.

The first simulation uses a resolution of $\Delta r = 300$ km $= 0.76\ d_i$. The proton cyclotron instability is identified by the pro-

275   duction of left-hand circularly polarised waves around the ion cyclotron frequency, with properties consistent to that of Alfvén Ion Cyclotron waves. The VDFs have a nearly bi-Maxwellian shape in all directions, indicating isotropization of the species. We also observe mirror modes in the middle of the magnetosheath, although with a lower growth rate, indicating that they grow further upstream. This resolution allows the proton cyclotron and mirror instabilities to grow adequately.

The second simulation uses a resolution of $\Delta r = 600$ km $= 0.37\ d_i$. The AIC waves are still present at this resolution, yet

280   not completely resolved. The VDFs are still nearly bi-Maxwellian, with a small loss-cone starting to appear, due to the presence of a growing mirror instability. The temperature anisotropy is hence larger than at the previous resolution. Even though the growth rate is larger than at $\Delta r = 300$ km, the resolution does not allow the maximum growth rate of the proton cyclotron instability to be reached.

The third simulation uses a resolution of $\Delta r = 900$ km $= 0.25\ d_i$. Large structures are observed, and the VDFs display a

285   significant loss-cone in the parallel directions. The anti-correlation of the fluctuations in magnetic field and density highlights the presence of mirror modes. In this simulation the temperature anisotropy is much larger than at higher resolutions. This is because the AIC waves are not present anymore. This resolution does to not resolve a spectrum of wave vectors large enough to allow the instability to grow.

This work shows that the proton cyclotron instability does not develop at low spatial resolution. Energy dissipation processes

290   are missing and thus the velocity distribution functions are not isotropized. Larger simulations with inhomogeneous spatial resolution scale should include a sub-grid model, like velocity space diffusion. This would account for the effects of the proton cyclotron instability without a significant increase of numerical resources.

Annales
Geophysicae

Discussions

Open Access

EGU

At the highest resolution, the proton cyclotron instability is well resolved. The proton cyclotron instability and the mirror instability being the two competing instabilities in this simulation, we conclude that there is no need to increase the spatial

295   resolution of a simulation beyond $\Delta r = 300$ km $= 0.76\ d_i$ at the cost of numerical resources, for the study of these instabilities. We also conclude that the resolution $\Delta r \approx 440$ km $= 0.6\ d_i$ would still give an adequate description of the proton cyclotron instability and therefore is an acceptable minimum spatial resolution for a simulation to study magnetosheath waves.
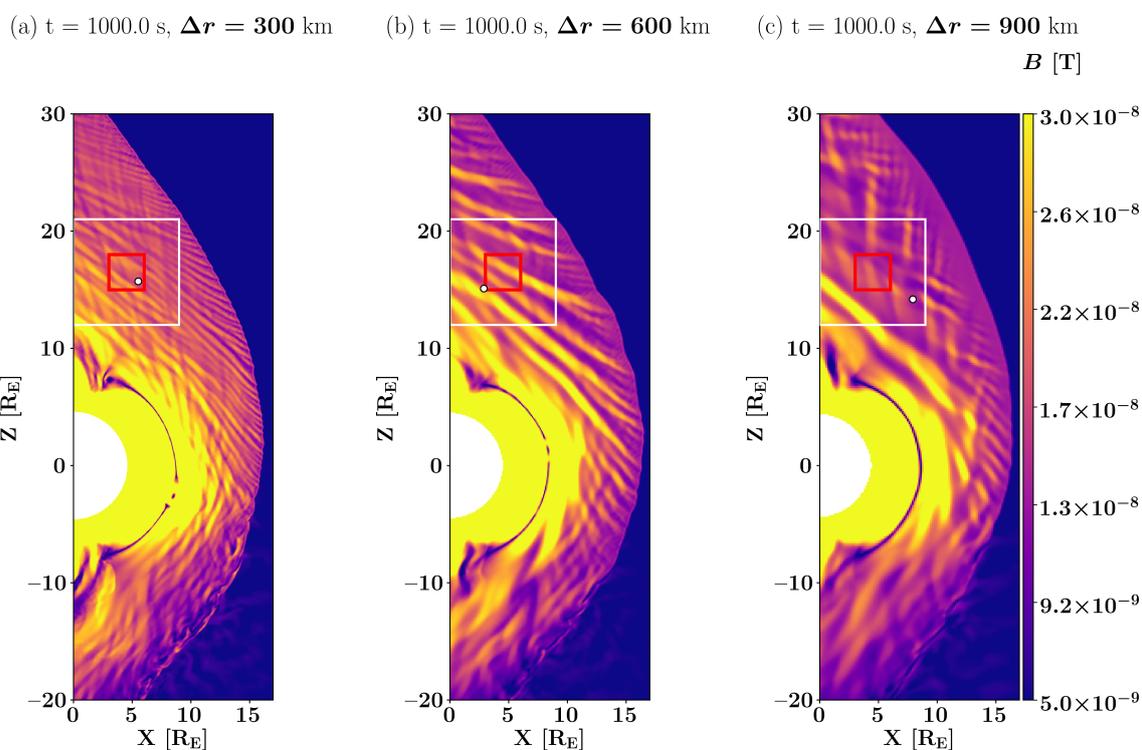
Figure 1. Global overview of the simulation setup with three different spatial resolutions: (a) $\Delta r = 300$ km, (b) $\Delta r = 600$ km and (c) $\Delta r = 900$ km. The colormap in each run is the magnitude of the magnetic field. The white square displays the area we focus on in the magnetosheath in the rest of the study. The red square displays the area where the FFT in Fig. 2 is performed. The black and white dot displays the location where data are taken for Fig. 3, 4, 5, 6, and the VDFs in Fig. 8.
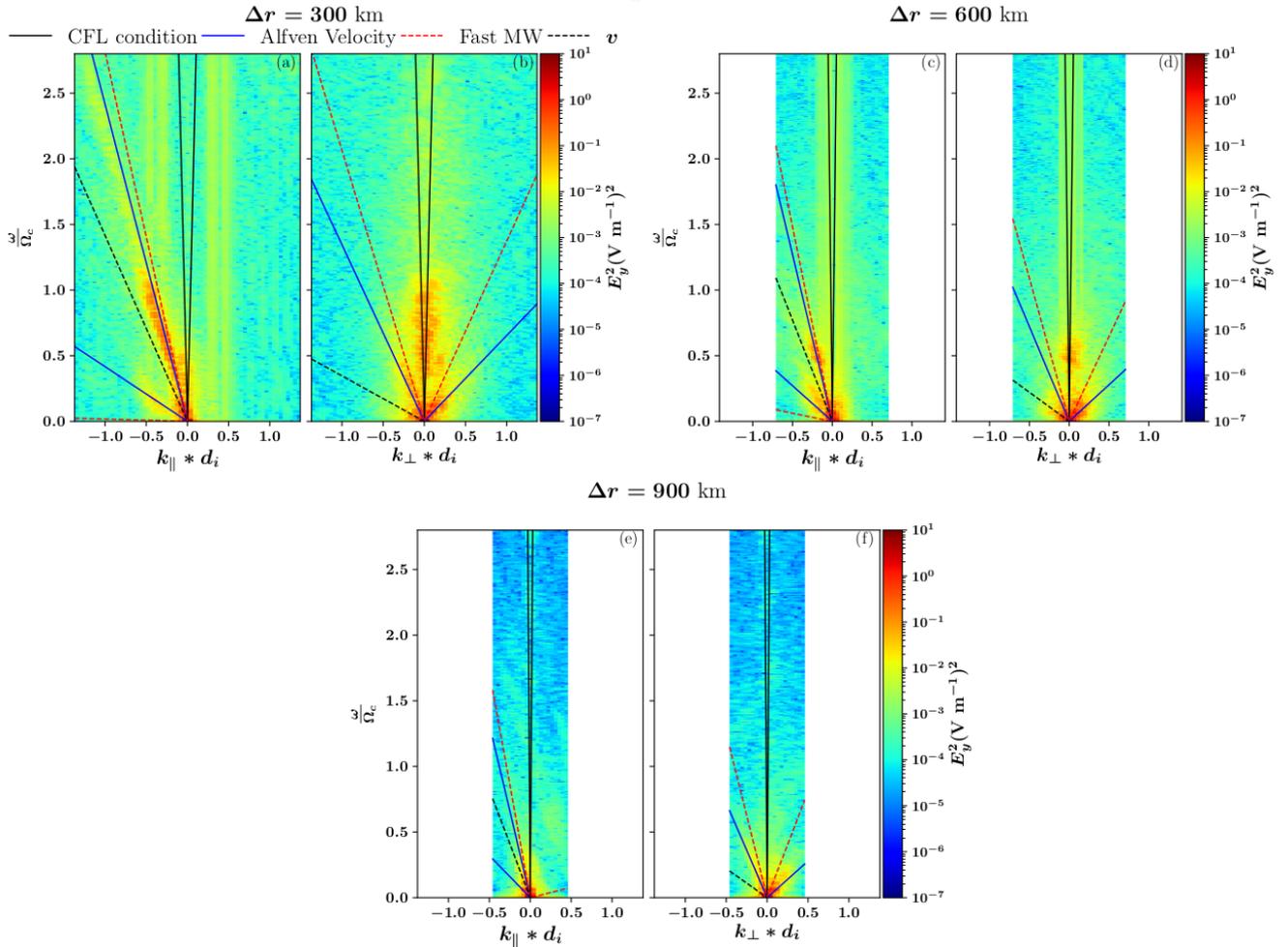
Figure 2. 2D Fast Fourier Transform of the y-component of the electric field in the direction parallel and perpendicular to the background magnetic field, at the location depicted by a red square in Fig. 1. Panels (a) and (b) display the results for the run at resolution $\Delta r = 300$ km, panels (c) and (d) the results for the run at resolution $\Delta r = 600$ km, and panels (e) and (f) the results for the run at resolution $\Delta r = 900$ km. The solid black lines represent the Courant-Friedrichs-Lewy condition, the solid blue lines the Alfvén speed, the dashed red lines the fast magnetosonic speed (labelled MW), with all wave frequencies shown in the simulation frame. The dashed black lines show the Doppler shift due to the plasma bulk flow.
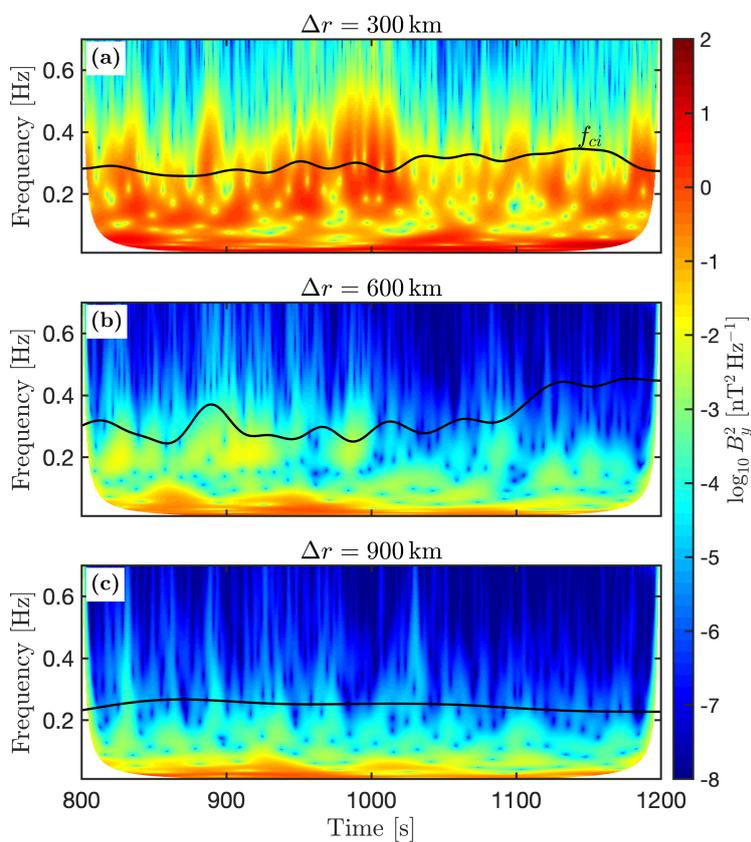
Figure 3. Wavelet analysis of the magnetic field for the virtual space craft locations given in Fig. 1. The colour background represents the power spectrum density of the y-component of the magnetic field. Panels (a) displays the results for the run at resolution $\Delta r = 300$ km, panel (b) the run at resolution $\Delta r = 600$ km, and panel (c) the run at resolution $\Delta r = 900$ km. The black curve on each plot indicates the proton cyclotron frequency.
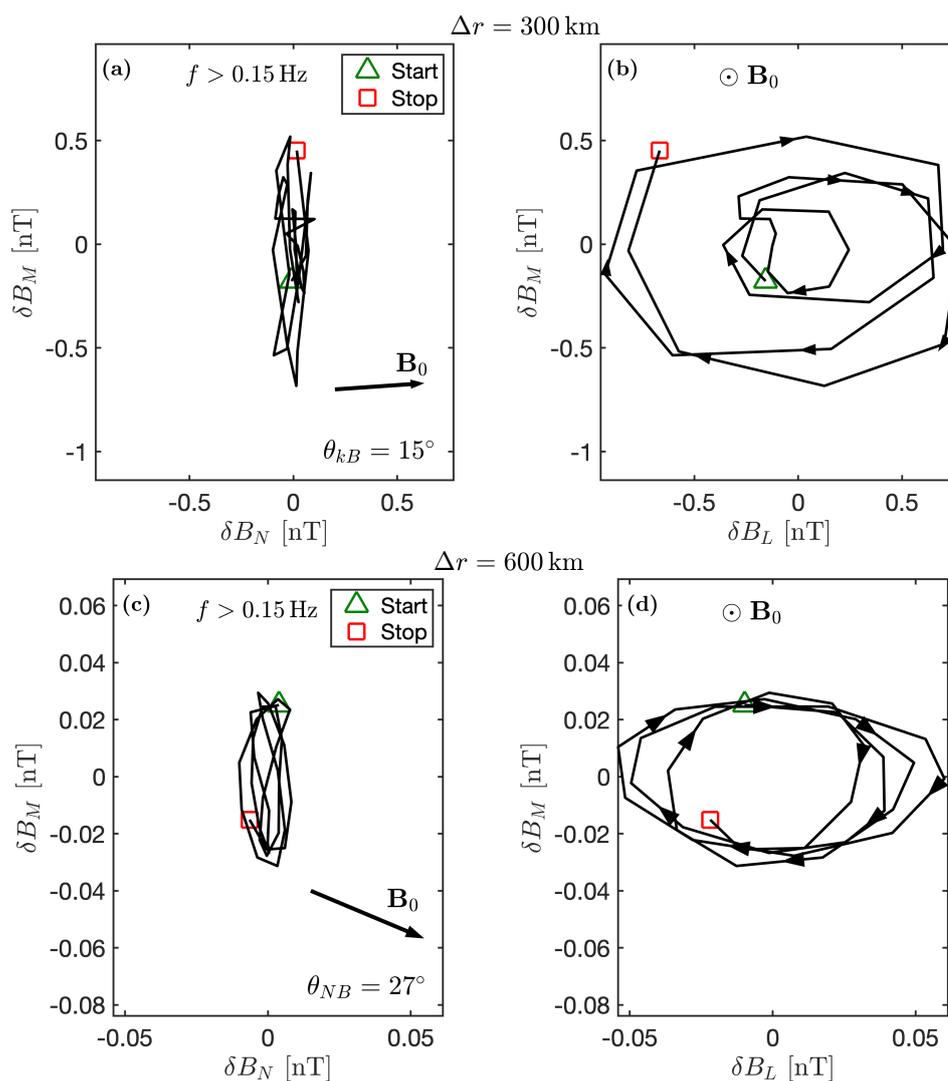
Figure 4. Hodogram of the magnetic field fluctuations. Panels (a) and (b) display the case $\Delta r = 300$ km, taken between $t = 996.5$ s and $t = 1013.5$ s. Panels (c) and (d) display the case $\Delta r = 600$ km, taken between $t = 910.0$ s and $t = 928.0$ s. Panels (a) and (c): intermediate (δB_M) and minimum (δB_N) variance directions. An arrow marks the average background field $\mathbf{B}_0$. Panels (b) and (d): intermediate (δB_M) and maximum (δB_L) variance directions. Arrows show the time evolution of the fluctuations. A green triangle marks the start of the interval and a red square marks the end.
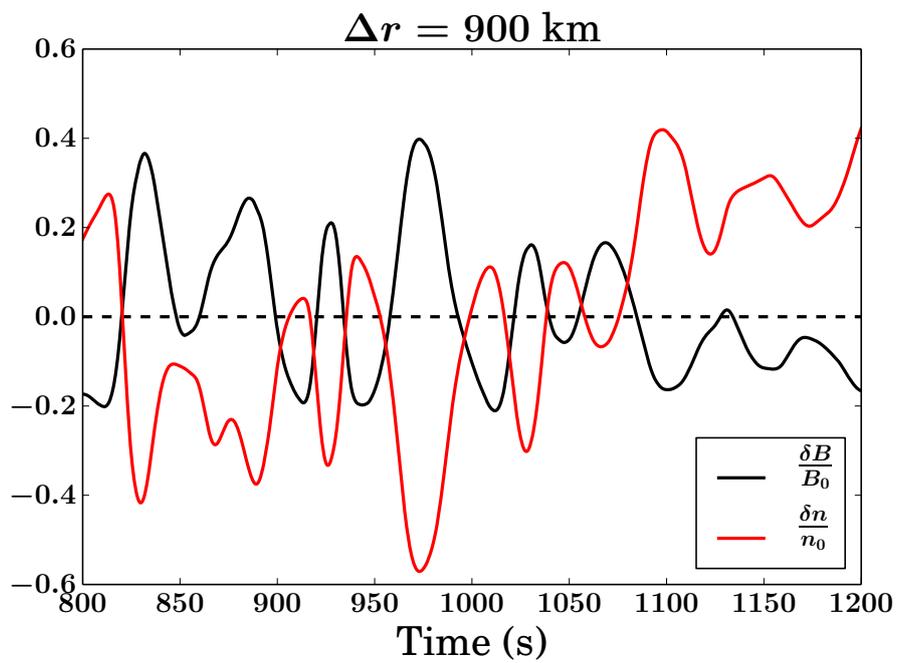
Figure 5. Magnetic field (black) and density (red) fluctuations for the run with resolution $\Delta r = 900$ km, measured at the virtual spacecraft location indicated by a black and white dot in Fig. 1.
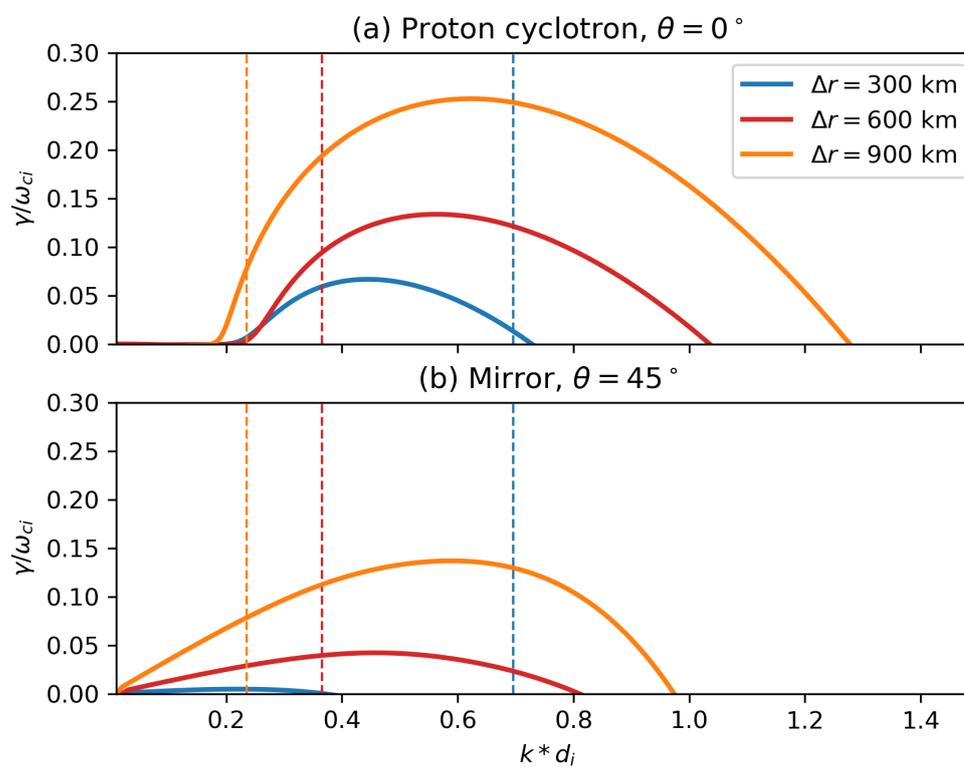
Figure 6. Growth rates γ of the proton cyclotron (panel (a)) and Mirror (panel (b)) instabilities calculated by HYDROS for the three different spatial resolutions: $\Delta r = 300$ km (blue), $\Delta r = 600$ km (red) and $\Delta r = 900$ km (orange). The dashed lines represent the maximum wave number $k_{\mathrm{max}} = \pi/2\Delta r$ which can be resolved by the model to get a proper description of the signal at each resolution.
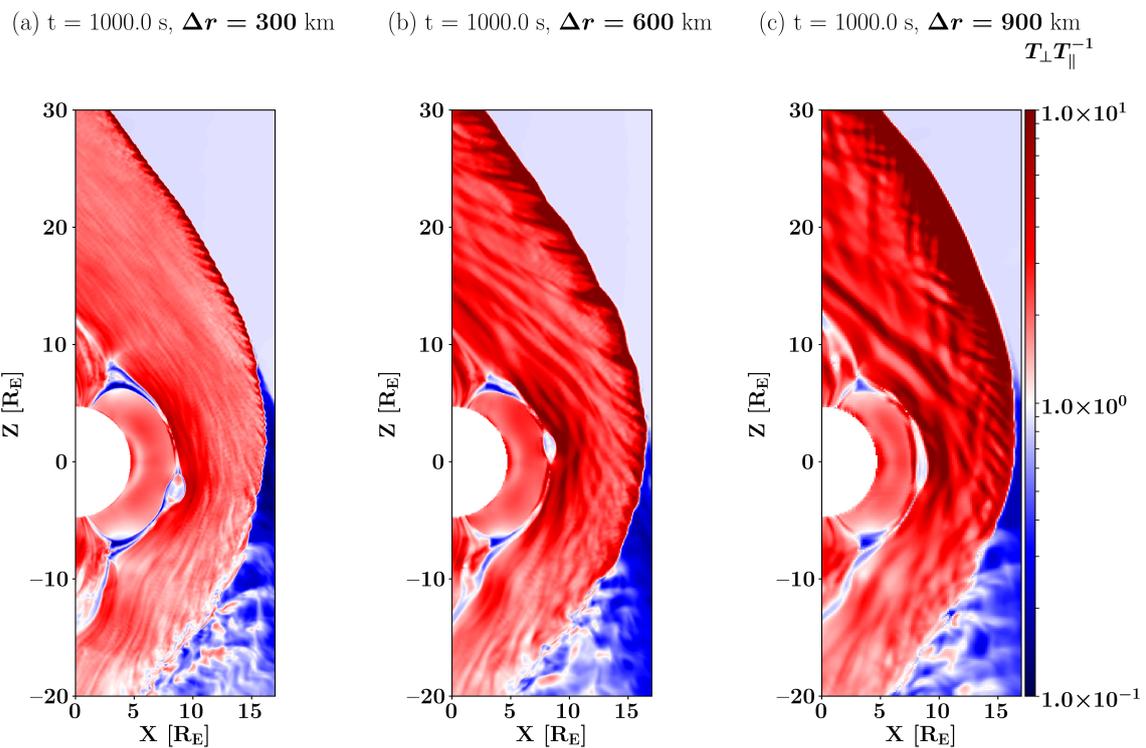
Figure 7. Temperature anisotropy for the resolution: (a) $\Delta r = 300$ km, (b) $\Delta r = 600$ km, (c) $\Delta r = 900$ km.
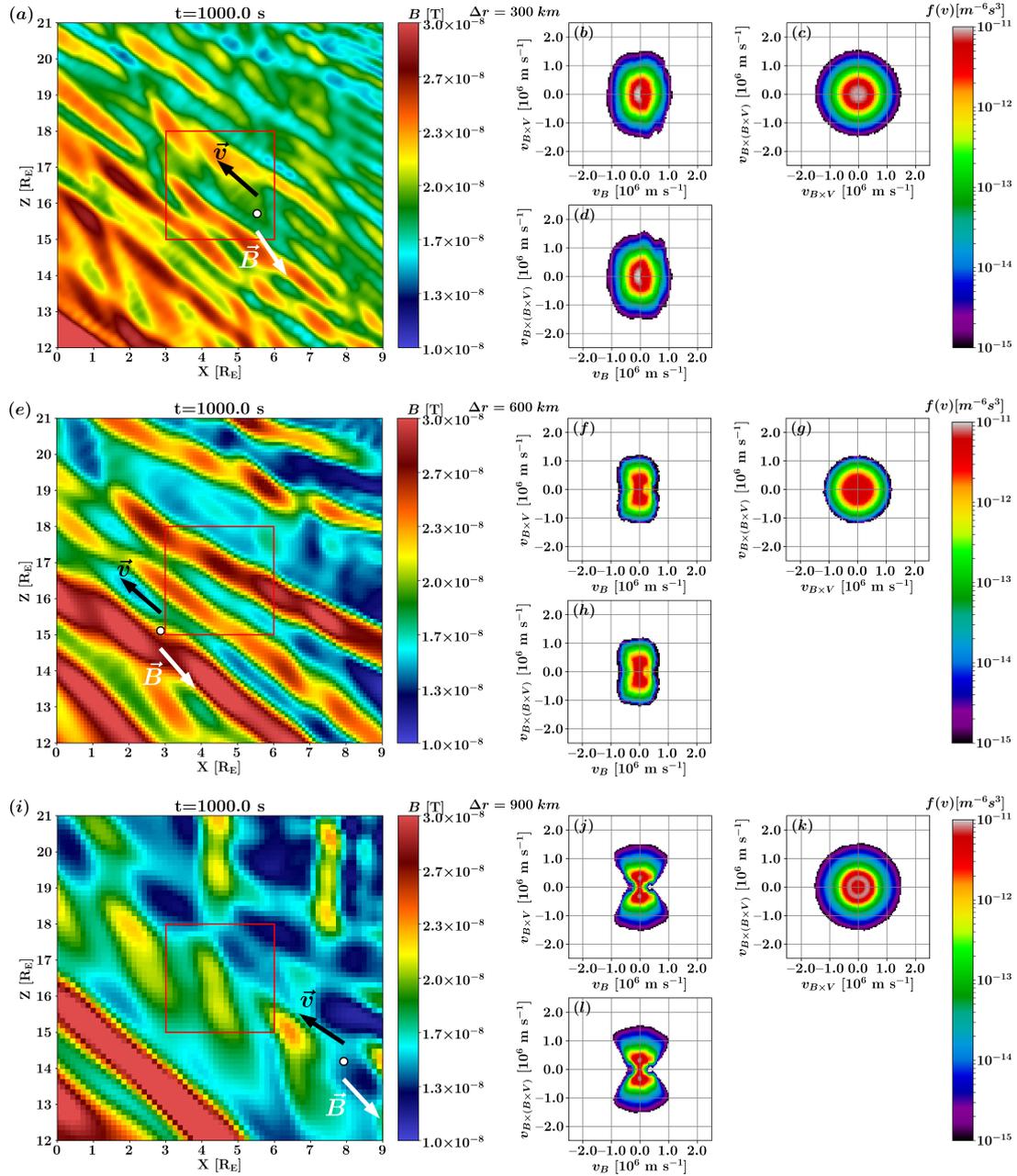
Figure 8. Colormap of the magnetic field (left) and velocity distribution functions in the three directions (right) located at the black and white circle. Panels (a)-(d) display the run with resolution $\Delta r = 300$ km, panels (e)-(h) the run with resolution $\Delta r = 600$ km and panels (i)-(l) the run with resolution $\Delta r = 900$ km. The black arrow displays the plasma bulk velocity and the white arrow displays the magnetic field direction, both taken at the location indicated by the black and white circle. The red square displays the area where the 2D-FFT is taken (Fig. 2).

Annales
Geophysicae
Discussions

Table 1. Summary table for each run with spatial resolutions, the inertial length d_i in the solar wind, the maximum wave vector allowed by the simulation $k_{\mathrm{max}} = \pi/\Delta r$, the wave vector at which the proton cyclotron instability's growth rate is maximum $k_{\gamma_{\mathrm{max}}}$, status of the proton cyclotron and mirror instabilities in the simulation, VDF shapes in the ($\mathbf{v_B}$, $\mathbf{v_{B} \times v}$) plane (Fig. 8b, f and j), temperature anisotropy, and plasma beta taken at the location indicated in Fig. 1 averaged over the time range used in this study.

Δr (km)	d_i (km)	$k_{\mathrm{max}}d_i$	$k_{\gamma_{\mathrm{max}}}d_i$	Proton cyclotron	Mirror	VDF ($\mathbf{v_B}$, $\mathbf{v_{B} \times v}$)	$T_\perp/T_\parallel$	β
300	228	0.68	0.44	yes	yes	Bi-Maxwellian	1.97	2.58
600	228	0.35	0.53	partially	yes	Nearly bi-Maxwellian beginning of loss-cone	2.56	2.72
900	228	0.23	0.63	no	yes	Loss-cone	3.41	4.18

305   *Video supplement.* TEXT

Author contributions. MD carried out most of the study and the writing of the paper. UG and YP-K participated in running the different simulations and the development of the analysis methods. MB participated in the development of the analysis methods. AO, MG, AJ and LT contributed in the data analysis and discussions. MP is the PI of the Vlasiator model and gave input on the interpretation of the simulation results. All co-authors participated in the discussion of the results and contributed in improving the manuscript.

310   *Competing interests.* The authors declare they have no conflicts of interest.

References

Ala-Lahti, M., Kilpua, E. K. J., Souček, J., Pulkkinen, T. I., and Dimmock, A. P.: Alfvén Ion Cyclotron Waves in Sheath Regions Driven by Interplanetary Coronal Mass Ejections, Journal of Geophysical Research: Space Physics, 124, 3893–3909, https://doi.org/10.1029/2019JA026579, 2019.

Alfvén, H.: Existence of Electromagnetic-Hydrodynamic Waves, Nature, 150, 405–406, https://doi.org/10.1038/150405d0, 1942.

Anderson, B. J. and Fuselier, S. A.: Magnetic pulsations from 0.1 to 4.0 Hz and associated plasma properties in the Earth's subsolar magnetosheath and plasma depletion layer, Journal of Geophysical Research: Space Physics, 98, 1461–1479, https://doi.org/10.1029/92JA02197, 1993.

Anderson, B. J., Denton, R. E., and Fuselier, S. A.: On determining polarization characteristics of ion cyclotron wave magnetic field fluctuations, Journal of Geophysical Research: Space Physics, 101, 13 195–13 213, https://doi.org/10.1029/96JA00633, 1996.

Blanco-Cano, X., Battarbee, M., Turc, L., Dimmock, A. P., Kilpua, E. K. J., Hoilijoki, S., Ganse, U., Sibeck, D. G., Cassak, P. A., Fear, R. C., Jarvinen, R., Juusola, L., Pfau-Kempf, Y., Vainio, R., and Palmroth, M.: Cavitons and spontaneous hot flow anomalies in a hybrid-Vlasov global magnetospheric simulation, Ann. Geophys., 36, 1081–1097, https://doi.org/10.5194/angeo-36-1081-2018, 2018.

Chandrasekhar, S., Kaufman, A. N., and Watson, K. M.: The Stability of the Pinch, Proceedings of the Royal Society of London. Series A, Mathematical and Physical Sciences, 245, 435–455, https://doi.org/10.2307/100290, 1958.

Childs, H., Brugger, E., Whitlock, B., Meredith, J., Ahern, S., Pugmire, D., Biagas, K., Miller, M., Harrison, C., Weber, G. H., Krishnan, H., Fogal, T., Sanderson, A., Garth, C., Bethel, E. W., Camp, D., Rübel, O., Durant, M., Favre, J. M., and Navrátil, P.: VisIt: An End-User Tool For Visualizing and Analyzing Very Large Data, in: High Performance Visualization–Enabling Extreme-Scale Scientific Insight, pp. 357–372, Chapman & Hall/CRC Press, 2012.

Davidson, R. C. and Ogden, J. M.: Electromagnetic ion cyclotron instability driven by ion energy anisotropy in high-beta plasmas, Physics of Fluids, 18, 1045–1050, https://doi.org/10.1063/1.861253, 1975.

Gary, S. P.: The mirror and ion cyclotron anisotropy instabilities, Journal of Geophysical Research: Space Physics, 97, 8519–8529, https://doi.org/10.1029/92JA00299, 1992.

Gary, S. P. and Winske, D.: Simulations of ion cyclotron anisotropy instabilities in the terrestrial magnetosheath, Journal of Geophysical Research: Space Physics, 98, 9171–9179, https://doi.org/10.1029/93JA00272, 1993.

Gary, S. P., Fuselier, S. A., and Anderson, B. J.: Ion anisotropy instabilities in the magnetosheath, Journal of Geophysical Research: Space Physics, 98, 1481–1488, https://doi.org/10.1029/92JA01844, 1993.

Grandin, M., Battarbee, M., Osmane, A., Ganse, U., Pfau-Kempf, Y., Turc, L., Brito, T., Koskela, T., Dubart, M., and Palmroth, M.: Hybrid-Vlasov modelling of nightside auroral proton precipitation during southward interplanetary magnetic field conditions, Annales Geophysicae, 37, 791–806, https://doi.org/10.5194/angeo-37-791-2019, 2019.

Görler, T., Lapillonne, X., Brunner, S., Dannert, T., Jenko, F., Merz, F., and T., T.: The global version of the gyrokinetic turbulence code GENE, Journal of Computational Physics, 230, 7053–7071, https://doi.org/10.1016/j.jcp.2011.05.034., 2011.

Hasegawa, A.: Drift Mirror Instability in the Magnetosphere, The Physics of Fluids, 12, 2642–2650, https://doi.org/10.1063/1.1692407, 1969.

Hellinger, P., Trávníček, P., Kasper, J. C., and Lazarus, A. J.: Solar wind proton temperature anisotropy: Linear theory and WIND/SWE observations, Geophysical Research Letters, 33, https://doi.org/10.1029/2006GL025925, 2006.

Hoilijoki, S., Palmroth, M., Walsh, B. M., Pfau-Kempf, Y., von Alfthan, S., Ganse, U., Hannuksela, O., and Vainio, R.: Mirror modes in the Earth's magnetosheath: Results from a global hybrid-Vlasov simulation, Journal of Geophysical Research: Space Physics, 121,

355 https://doi.org/10.1002/2015JA022026, 2016.

Hoilijoki, S., Ganse, U., Sibeck, D. G., Cassak, P. A., Turc, L., Battarbee, M., Fear, R. C., Blanco-Cano, X., Dimmock, A. P., Kilpua, E. K. J., Jarvinen, R., Juusola, L., Pfau-Kempf, Y., and Palmroth, M.: Properties of Magnetic Reconnection and FTEs on the Dayside Magnetopause With and Without Positive IMF Bx Component During Southward IMF, Journal of Geophysical Research: Space Physics, 124, 4037–4048, https://doi.org/10.1029/2019JA026821, 2019.

360 Ichimaru, S.: Basic Principles of Plasma Physics: a Statistical Approach, Addison-Wesley, 1980.

Kempf, Y., Pokhotelov, D., Gutynska, O., Wilson III, L. B., Walsh, B. M., von Alfthan, S., Hannuksela, O., Sibeck, D. G., and Palmroth, M.: Ion distributions in the Earth's foreshock: Hybrid-Vlasov simulation and THEMIS observations, Journal of Geophysical Research: Space Physics, 120, 3684–3701, https://doi.org/10.1002/2014JA020519, 2015.

Kivelson, M. G. and Southwood, D. J.: Mirror instability II: The mechanism of nonlinear saturation, Journal of Geophysical Research: Space

365 Physics, 101, 17 365–17 371, https://doi.org/10.1029/96JA01407, 1996.

Lacombe, C., Belmont, G., D, H., Harvey, C., Mangeney, A., Russell, C., Gosling, J., and Fuselier, S.: Density and magnetic field fluctuations observed by ISEE 1-2 in the quiet magnetosheath, Annales Geophysicae, 13, 343–357, https://doi.org/10.1007/s005850050170, 1994.

McKean, M. E., Winske, D., and Gary, S. P.: Mirror and ion cyclotron anisotropy instabilities in the magnetosheath, Journal of Geophysical Research: Space Physics, 97, 19 421–19 432, https://doi.org/10.1029/92JA01842, 1992.

370 McKean, M. E., Winske, D., and Gary, S. P.: Two-dimensional simulations of ion anisotropy instabilities in the magnetosheath, Journal of Geophysical Research: Space Physics, 99, 11 141–11 153, https://doi.org/10.1029/93JA03025, 1994.

Palmroth, M., Honkonen, I., Sandroos, A., Kempf, Y., von Alfthan, S., and Pokhotelov, D.: Preliminary testing of global hybrid-Vlasov simulation: Magnetosheath and cusps under northward interplanetary magnetic field, Journal of Atmospheric and Solar-Terrestrial Physics, 99, 41 – 46, https://doi.org/10.1016/j.jastp.2012.09.013, 2013.

375 Palmroth, M., Ganse, U., Pfau-Kempf, Y., Battarbee, M., Turc, L., Brito, T., Grandin, M., Hoilijoki, S., Sandroos, A., and von Alfthan, S.: Vlasov methods in space physics and astrophysics, Living Reviews in Computational Astrophysics, 4, https://doi.org/10.1007/s41115-018-0003-2, 2018.

Palmroth, M., Hietala, H., Plaschke, F., Archer, M., Karlsson, T., Blanco-Cano, X., Sibeck, D., Kajdič, P., Ganse, U., Pfau-Kempf, Y., Battarbee, M., and Turc, L.: Magnetosheath jet properties and evolution as determined by a global hybrid-Vlasov simulation, Annales

380 Geophysicae, 36, 1171–1182, https://doi.org/10.5194/angeo-36-1171-2018, 2018.

Pfau-Kempf, Y., Battarbee, M., Ganse, U., Hoilijoki, S., Turc, L., von Alfthan, S., Vainio, R., and Palmroth, M.: On the Importance of Spatial and Velocity Resolution in the Hybrid-Vlasov Modeling of Collisionless Shocks, Frontiers in Physics, 6, 44, https://doi.org/10.3389/fphy.2018.00044, 2018.

Pomoell, J. and Poedts, S.: EUHFORIA: European heliospheric forecasting information asset, J. Space Weather Space Clim., 8, A35,

385 https://doi.org/10.1051/swsc/2018020, 2018.

Rakhmanova, L. S., Riazantseva, M. O., Zastenker, G. N., and Yermolaev, Y. I.: High-frequency plasma fluctuations in the middle magnetosheath and near its boundaries: Spektr-R observations, Journal of Plasma Physics, 83, 705830 204, https://doi.org/10.1017/S002237781700023X, 2017.

Revel, A., Minea, T., and Costin, C.: 2D PIC-MCC simulations of magnetron plasma in HiPIMS regime with external circuit, Plasma Sources

390 Science and Technology, 27, 105 009, https://doi.org/10.1088/1361-6595/aadebe, 2018.

Schwartz, S. J., Burgess, D., and Moses, J. J.: Low-frequency waves in the Earth's magnetosheath: present status, Annales Geophysicae, 14, 1134–1150, https://doi.org/10.1007/s00585-996-1134-z, 1997.

Seough, J., Yoon, P. H., and Hwang, J.: Simulation and quasilinear theory of proton firehose instability, Physics of Plasmas, 22, https://doi.org/10.1063/1.4905230, 2015.

395 Sonnerup, B. U. Ö. and Scheible, M.: Minimum and Maximum Variance Analysis, ISSI Scientific Reports Series, 1, 185–220, 1998.

Soucek, J., Lucek, E., and Dandouras, I.: Properties of magnetosheath mirror modes observed by Cluster and their response to changes in plasma parameters, Journal of Geophysical Research: Space Physics (1978–2012), 113, https://doi.org/10.1029/2007JA012649, 2008.

Soucek, J., Escoubet, C. P., and Grison, B.: Magnetosheath plasma stability and ULF wave occurrence as a function of location in the magnetosheath and upstream bow shock parameters, Journal of Geophysical Research: Space Physics, 120, 2838–2850,
400 https://doi.org/10.1002/2015JA021087, 2015.

Southwood, D. J. and Kivelson, M. G.: Mirror instability: 1. Physical mechanism of linear instability, Journal of Geophysical Research: Space Physics, 98, 9181–9187, https://doi.org/10.1029/92JA02837, 1993.

Tanaka, M.: Simulations of heavy ion heating by electromagnetic ion cyclotron waves driven by proton temperature anisotropies, Journal of Geophysical Research: Space Physics, 90, 6459–6468, https://doi.org/10.1029/JA090iA07p06459, 1985.

405 Told, D., Cookmeyer, J., Astfalk, P., and Jenko, F.: A linear dispersion relation for the hybrid kinetic-ion/fluid-electron model of plasma physics, New Journal of Physics, 18, 075 001, https://doi.org/10.1088/1367-2630/18/7/075001, 2016.

Torrence, C. and Compo, G. P.: A Practical Guide to Wavelet Analysis, Bulletin of the American Meteorological Society, 79, 61–78, https://doi.org/10.1175/1520-0477(1998)079<0061:APGTWA>2.0.CO;2, 1998.

Tsurutani, B. T., Smith, E. J., Anderson, R. R., Ogilvie, K. W., Scudder, J. D., Baker, D. N., and Bame, S. J.: Lion roars
410 and nonoscillatory drift mirror waves in the magnetosheath, Journal of Geophysical Research: Space Physics, 87, 6060–6072, https://doi.org/10.1029/JA087iA08p06060, 1982.

Turc, L., Ganse, U., Pfau-Kempf, Y., Hoilijoki, S., Battarbee, M., Juusola, L., Jarvinen, R., Brito, T., Grandin, M., and Palmroth, M.: Foreshock Properties at Typical and Enhanced Interplanetary Magnetic Field Strengths: Results From Hybrid-Vlasov Simulations, Journal of Geophysical Research: Space Physics, 123, 5476–5493, https://doi.org/10.1029/2018JA025466.

415 von Alfthan, S., Pokhotelov, D., Kempf, Y., Hoilijoki, S., Honkonen, I., Sandroos, A., and Palmroth, M.: Vlasiator: First global hybrid-Vlasov simulations of Earth's foreshock and magnetosheath, Journal of Atmospheric and Solar-Terrestrial Physics, 120, 24 – 35, https://doi.org/10.1016/j.jastp.2014.08.012, 2014.

Williams, D. J., Mitchell, D. G., Frank, L. A., and Eastman, T. E.: Three-dimensional magnetosheath plasma ion distributions from 200 eV to 2 MeV, Journal of Geophysical Research: Space Physics, 93, 12 783–12 794, https://doi.org/10.1029/JA093iA11p12783, 1988.

420 Zhao, J., Wang, T., Graham, D. B., He, J., Liu, W., Dunlop, M. W., and Wu, D.: Identification of the Nature of Electromagnetic Waves near the Proton-cyclotron Frequency in Solar-terrestrial Plasmas, The Astrophysical Journal, 890, 17, https://doi.org/10.3847/1538-4357/ab672f, 2020.